

Review

Principles of deep immunohistochemistry for 3D histology

Chun Ngo Yau,^{1,2,3,7} Hei Ming Lai,^{1,2,3,4,6,7,*} Krit Lee,¹ Andrew J. Kwok,^{2,3,4,6} Junzhe Huang,^{2,3,4,6} and Ho Ko^{1,2,3,4,5,6,*}¹Department of Psychiatry, The Chinese University of Hong Kong, Shatin, New Territories, Hong Kong SAR, China²Department of Medicine and Therapeutics, The Chinese University of Hong Kong, Shatin, New Territories, Hong Kong SAR, China³Li Ka Shing Institute of Health Sciences, The Chinese University of Hong Kong, Shatin, New Territories, Hong Kong SAR, China⁴Margaret K.L. Cheung Research Centre for Management of Parkinsonism, The Chinese University of Hong Kong, Shatin, New Territories, Hong Kong SAR, China⁵School of Biomedical Sciences, Faculty of Medicine, The Chinese University of Hong Kong, Shatin, New Territories, Hong Kong SAR, China⁶Gerald Choa Neuroscience Institute, The Chinese University of Hong Kong, Shatin, New Territories, Hong Kong SAR, China⁷These authors contributed equally*Correspondence: hmlai@cuhk.edu.hk (H.M.L.), ho.ko@cuhk.edu.hk (H.K.)<https://doi.org/10.1016/j.crmeth.2023.100458>

SUMMARY

Deep immunohistochemistry (IHC) is a nascent field in three-dimensional (3D) histology that seeks to achieve thorough, homogeneous, and specific staining of intact tissues for visualization of microscopic architectures and molecular compositions at large spatial scales. Despite the tremendous potential of deep IHC in revealing molecule-structure-function relationships in biology and establishing diagnostic and prognostic features for pathological samples in clinical practice, the complexities and variations in methodologies may hinder its use by interested users. We provide a unified framework of deep immunostaining techniques by discussing the theoretical considerations of the physicochemical processes involved, summarizing the principles applied in contemporary methods, advocating a standardized benchmarking scheme, and highlighting unaddressed issues and future directions. By providing the essential information to guide investigators in customizing immunolabeling pipelines, we also seek to facilitate the adoption of deep IHC for researchers to address a wide range of research questions.

INTRODUCTION

The promises of three-dimensional (3D) histology in modern biology

3D histology is the new frontier for tissue-based research and clinical diagnostics, facilitated by maturing technologies in the required core technical components: tissue processing, fluorescent probes, deep penetrating tissue staining, microscopy, and large-volume image processing. The ability to visualize molecules and structures throughout tissue blocks promises to advance holistic systems biology research and could be potentially applied to routine clinical use. Ongoing efforts to pioneer the applications of 3D histology to diverse problems as well as tackle the remaining obstacles to achieve cost-efficient, automatable 3D histology pipelines are therefore gaining momentum in the field.

The strengths of 3D histology include permitting reconstruction of microstructural details that are otherwise hard to appreciate in two-dimensional images, unbiased sampling of cells and molecules in tissues, and a much higher data throughput. For example, in neural circuit tracing, complete quantification of input projection neurons to a given brain region as well as tracing of inter-regional axonal tracts are only feasible with high-throughput 3D labeling and imaging. Knowledge gained

from these experiments is crucial for revealing the fundamental rules of neuronal connectivity and constraining neural circuit models. Volumetric histology also allows reconstruction of microvascular networks in different organs, from the brain to the kidney, informing us of the basic principles governing their organization and the underlying processes that mediate normal or compromised tissue perfusion in health and disease. Apart from elucidating structure-function relationships in fundamental research, 3D histology may also reduce the chance for pathologists and clinicians to miss features of malignancy in tissue samples relevant to prognostication or treatment decisions.

The obstacle of limited probe penetration in 3D immunostaining

There are two general approaches to obtain whole-tissue-block 3D images: either through serial physical sectioning or via optical sectioning microscopy after tissue clearing. Both methods date back over 100 years.^{1,2} In serial sectioning tomography, tissues are systematically sectioned into a series of thin slices, imaged, and reconstructed *in silico*. Alternatively, tissues can be turned optically transparent via tissue clearing, after which they can be imaged with optical sectioning microscopy. In both cases, the structures and molecules of the tissue must be visualized through appropriate staining methods. In particular, deep



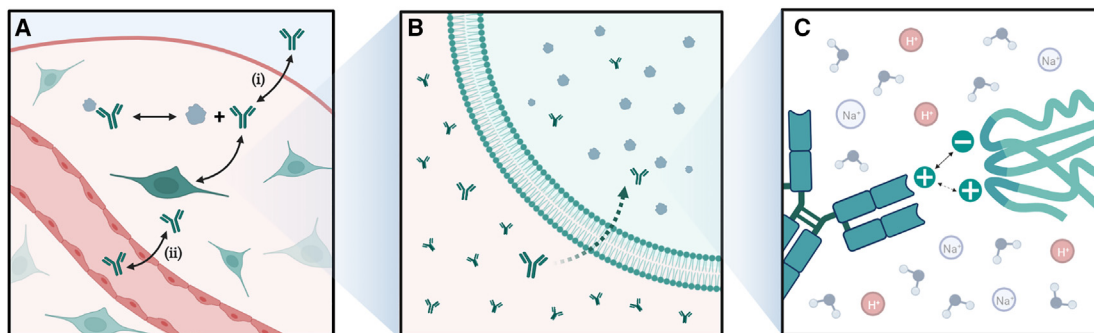


Figure 1. An overview of the RDA process in deep immunostaining

(A) Diffusion and advective transport of Abs into the tissue. The effective path from Abs to Ags through cell membranes and the ECM forms the main diffusion barrier (curved arrows), while binding reactions with peripheral Ags form the main reaction barrier (straight arrow). There are two major routes for Abs in the staining buffer (blue) to reach the intra- and extracellular Ags: (i) directly diffusing from the tissue surface and (ii) via the low-resistance tissue vasculature (if intact and patent). Both require diffusion through the dense tissue matrix (pink). The reaction barrier for route (ii) is omitted for simplicity.

(B) Penetration of the cell membrane to access intracellular Ags. Without permeabilization, the intact cell membrane acts as a significant barrier to hinder Ab access to intracellular Ags. Extracellular Ags are omitted for simplicity.

(C) Ab-Ag reaction and its determinants. Ab-Ag reaction is largely determined by the properties of the local environment, such as temperature, pH, and ionic strength. Alterations of these parameters can affect the non-covalent Ab-Ag interactions.

The figure was created with [BioRender](#).

penetrating immunohistochemistry (IHC) has demonstrated promising results in studying tissues from all domains of life when combined with the aforementioned approaches, especially in tissues where it is important to express endogenous fluorescent protein reporters. Crucially, combining deep penetrating IHC with 3D histology can label specific biomolecules to provide rich molecular information, which is complementary with small molecule dyes³ and other label-free approaches, such as micro-computed tomography,^{4,5} second-harmonic imaging microscopy,^{6,7} and ultra-high-resolution magnetic resonance imaging.^{8,9}

Despite the successes in automated serial sectioning tomography^{10–12} and tissue clearing,^{13–15} the insufficient penetration depth of antibodies in IHC remains a significant challenge in 3D histology. Without sufficient optimization, IHC of millimeter- or centimeter-scale tissues typically results in deposition of most antibodies in the periphery, leading to a large gradient of signals despite the tissue has turned visibly transparent. This rimming phenomenon hinders application of 3D histology to problems requiring quantitative analyses and comparisons. For example, when quantifying the expression level of specific proteins that impact tumor growth in different spatial locations of cancerous tissues or that of neuronal activation-associated immediate-early genes to identify active neurons participating in a given neurophysiological process across brain regions, attaining homogeneous staining for the proteins of interest located at different depths from the tissue surface is essential.

In this review, we provide a unified theoretical framework for the emerging field of deep IHC that seeks to overcome these challenges. We first perform an in-depth analysis of the two main processes in immunostaining: antibody movement across tissues and the subsequent antibody-antigen binding. After reviewing the determinants of these processes, we summarize and categorize the existing methodologies based on how they

manipulate different physicochemical parameters to achieve deep immunostaining. To foster consensus in data interpretation, we propose and advocate use of a standardized benchmarking scheme to allow stringent comparisons between methods. Last, we highlight future directions and unaddressed issues in the field. By providing essential information that guides researchers to systematically formulate solutions for unresolved challenges, we seek to facilitate the development and evaluation of unexplored approaches for deep immunostaining and 3D histology.

DEEP IMMUNOLABELING: THEORY

A quantitative framework of antibody movement in tissues

Devising strategies to improve antibody penetration requires us to consider factors determining antibody movements in tissues. Like all soluble molecular entities, unbound antibodies diffuse along concentration gradients and can be carried by advective transport. These processes need to overcome the diffusion barrier (Figures 1A and 1B), formed by tissue compositions (e.g., cell membrane, extracellular matrix [ECM]) along the path from the staining buffer to extra- and intracellular antigens in tissue. During the transport process, antibodies become immobilized upon binding to fixed tissue antigens (Ags). For a sufficiently dense Ag target, this becomes a significant reaction that depletes antibodies along the transport path in addition to other possible concurrent processes, such as denaturation or clumping, which are frequently observed in experiments. Together, these constitute the reaction barrier (Figure 1A). To increase mobile, functional antibody (Ab_f) concentration ($[Ab_f]_{r,t}$) at a certain spatial position (r) in the tissue, we consider how $[Ab_f]_{r,t}$ changes over time (t) based on these processes:

change in $[Ab_f]_{r,t} = - Ab_f$ depletion by various reactions + Ab_f diffusion + Ab_f advection.

In the most general form, the equation describing such a reaction-diffusion-advection (RDA) process is as follows:

$$\frac{\partial[\text{Ab}_f]_{r,t}}{\partial t} = -S + \nabla \cdot (D_{\text{eff}} \nabla [\text{Ab}_f]_{r,t}) - \nabla \cdot (\mathbf{v} [\text{Ab}_f]_{r,t}). \quad (\text{Equation 1})$$

Here, the first term S represents the sink term (i.e., loss of Ab_f with Ag binding and other possible reactions), D_{eff} denotes the Ab_f effective diffusivity in tissue (or effective diffusion coefficient, which can also vary with \mathbf{r} and t), \mathbf{v} is the Ab_f advective transport velocity field, ∇ and $\nabla \cdot$ are the gradient and divergence operators, respectively. For simplicity of notation, the subscripts will be dropped in subsequent expressions, and it is implicitly understood that the different concentration quantities depend on \mathbf{r} and t .

In the simplest form, in the absence of other entities that bind with either Ab_f or Ag , and assuming that no Ab_f clumping or denaturation occurs, S is given by

$$S = \frac{\partial[\text{Ab} - \text{Ag}]}{\partial t} = k_a [\text{Ab}_f][\text{Ag}] - k_d [\text{Ab} - \text{Ag}], \quad (\text{Equation 2})$$

where $[\text{Ab} - \text{Ag}]$ is the bound $\text{Ab} - \text{Ag}$ concentration, $[\text{Ag}]$ denotes accessible Ag concentration, and k_a and k_d correspond to $\text{Ab} - \text{Ag}$ association and dissociation rate constants, respectively. At equilibrium, $S = 0$, the ratio $K_{\text{eq}} = k_a/k_d$ gives the equilibrium constant of the reaction.

To allow easier analysis of system behavior, we may further consider the simpler case with a constant Ab_f effective diffusivity D_{eff} and Ab_f transport by incompressible advection, described by a simpler form of the RDA equation:

$$\frac{\partial[\text{Ab}_f]}{\partial t} = \{ -k_a [\text{Ab}_f][\text{Ag}] + k_d [\text{Ab} - \text{Ag}] \} + D_{\text{eff}} \nabla^2 [\text{Ab}_f] - \mathbf{v} \cdot \nabla [\text{Ab}_f]. \quad (\text{Equation 3})$$

where ∇^2 is the Laplace operator. Incorporating factors that determine the various parameters (discussed in later sections), the RDA model provides a quantitative framework that can be either solved analytically under simplified conditions or numerically simulated with appropriately set initial and boundary conditions to guide deep probe penetration method development, as exemplified by several prior studies.^{16–18}

This theoretical framework provides intuitive strategies to enhance immunolabeling depth, which is directly related to the attainable concentration of Ab_f s within the tissue matrix. These include (1) increasing Ab availability by simply increasing its concentration or reducing Ab depletion by temporarily inhibiting $\text{Ab} - \text{Ag}$ binding and enhancing their dissociation (i.e., modulating k_a and k_d in Equations 2 and 3 or, equivalently, K_{eq}), (2) enhancing the effective diffusivity in tissue (i.e., increasing D_{eff} in Equations 1 and 3) or reducing the distance to diffuse, and (3) increasing Ab transport by advective transport (i.e., creating and controlling \mathbf{v} in Equations 1 and 3). All existing 3D immunostaining approaches can be classified based on adoption of one or more of these strategies. In the following sections, we discuss the

theoretical considerations and state-of-the-art methods categorized by their main principle or approach adopted (Table 1).

FACTORS DETERMINING AB-AG INTERACTIONS

$\text{Ab} - \text{Ag}$ reaction is mediated by non-covalent forces, which contribute to its reversible nature and ultimately determine the K_{eq} . These forces are known to depend on numerous physico-chemical parameters, including temperature, pH, ionic strength, and the presence of detergent(s) in the reaction environment (Figure 1C). In general, because $\text{Ab} - \text{Ag}$ binding exhibits little dependence on the Ag tertiary structures, these factors can be interpreted as having a direct effect on the Ab 's tertiary folding and, hence, its ability to bind its target Ag , quantitatively measurable as K_{eq} . To reduce Ab depletion or decrease the magnitude of S , a rational approach is to reduce K_{eq} via manipulation of these parameters.

Temperature

Generally, the rate constant k of a given chemical reaction increases with the absolute temperature (T) and the relationship can be approximated by the Arrhenius equation

$$k = A e^{-\frac{E_a}{RT}}, \quad (\text{Equation 4})$$

where A is the pre-exponential factor (a constant scaling factor for a given reaction), E_a is the activation energy of the reaction, and R is the ideal gas constant. Provided that no denaturation occurs, an elevated temperature increases k_a and k_d . Because $\text{Ab} - \text{Ag}$ binding is exothermic, at higher temperatures, k_d tends to increase disproportionately over k_a , decreasing K_{eq} (i.e., favoring $\text{Ab} - \text{Ag}$ dissociation). For some Abs with direct measurements made, k_d increases by more than 20-fold between 1°C and 37°C, while k_a typically only increases a few times.²⁵ k_d is thus a major determinant of the binding affinity and its temperature dependence. It is, however, important to remember that such a relationship does not necessarily hold for all $\text{Ab} - \text{Ag}$ pairs across all temperature ranges because of the complex nature of their interactions. For $\text{Ab} - \text{Ag}$ pairs whose binding can be effectively inhibited by heating to above physiological temperatures, we still have to take into consideration possible heat denaturation of Abs and/or Ags .

Ionic strength

Electrostatic interactions between Abs and Ags facilitate their mutual attraction as they approach each other on the nanometer scale. These long-range forces are influenced by the ionic strength (and the pH; further discussed below) of the reaction medium. In a reaction medium with high ionic strength, the excess ions may cluster around the reactants and neutralize their charges, thereby interfering with their electrostatic interactions. Conversely, it has been shown that, under low ionic strength, the Ag binding of low-affinity Abs is significantly enhanced, while that of high-affinity Abs remains relatively constant.²⁶ Hence, one possible approach to reduce K_{eq} is to perform immunostaining in a medium with high ionic strength. Non-specific interactions between Abs and tissue proteins may also be reduced based on a similar mechanism.

Table 1. Overview of selected deep immunostaining methods

Main principle(s) employed	Method	Main strategy	Max. immunostaining scale(s) and sample type(s) shown (time required for immunolabeling)	Other compatible probe labeling modalities tested	Requires specialized equipment?	Automatable with pipette robots?	Remarks on applicability
Enhanced Ab diffusion	iDISCO ¹⁹	tissue treatment with methanol, dichloromethane, H ₂ O ₂ , DMSO	embryonic day 18.5 (E18.5) whole mouse embryo; whole adult mouse brain, kidney (3–4 days of incubation with 1° Ab; additional 3–4 days with 2° Ab)	endogenously expressed fluorescent proteins; EdU labeling with click chemistry detection; cholera toxin B subunit; TO-PRO-3	no	yes	–
	SHANEL ²⁰	tissue permeabilization with CHAPS, a zwitterionic detergent	1.5-cm-thick human brain slice (7 days of incubation with 1° Ab; additional 7 days with 2° Ab)	chemical dyes (TO-PRO-3, Methoxy-X04), lectin, TRITC-dextran	no	yes	–
Advective Ab transport	stochastic electrotransport (SE) ¹⁶	application of a rotating electric field to preferentially drive advective dispersion of Ab in tissue	whole adult mouse brain (1 day)	endogenously expressed fluorescent proteins	yes	no	equipment dependent; max. scale shown when combined with eFLASH

(Continued on next page)

Table 1. Continued

Main principle(s) employed	Method	Main strategy	Max. immunostaining scale(s) and sample type(s) shown (time required for immunolabeling)	Other compatible probe labeling modalities tested	Requires specialized equipment?	Automatable with pipette robots?	Remarks on applicability
Reduced Ab diffusion distance	vDISCO ²¹	high-pressure <i>in vivo</i> transcardial perfusion of nanobodies to reach deep-tissue regions	whole adult mouse body (11–13 days of transcardial perfusion with various decolorization, permeabilization, and staining solutions)	chemical/protein probes (DAPI, lectin)	no	no	requires training to perfect dissection and perfusion skills; endogenous fluorescence signals will be lost
	ELAST ²²	turning sample into reversibly stretchable tissue-hydrogel	whole adult mouse brain; 5-mm-thick human brain slice (1 day of tissue compression and relaxation cycles during staining; prior tissue-hydrogel transformation requires ~18 days)	chemical/protein probes (DAPI, lectin)	yes	no	requires manual embedding and careful handling of hydrogel-embedded tissues

(Continued on next page)

Table 1. Continued

Main principle(s) employed	Method	Main strategy	Max. immunostaining scale(s) and sample type(s) shown (time required for immunolabeling)	Other compatible probe labeling modalities tested	Requires specialized equipment?	Automatable with pipette robots?	Remarks on applicability
Transient inhibition of Ab-Ag binding	SWITCH ²³	using SDS for strong inhibition of Ab-Ag binding	whole adult mouse brain (7 days of incubation with pre-conjugated 2° Fab-1° Ab in SWITCH-OFF solution)	chemical/protein probes (DAPI, SYTO 16, lectin)	no	yes	–
	CUBIC-HV ¹⁷	using urea and Quadrol to modulate Ab-Ag binding	whole adult mouse brain; 1-cm ³ human cerebellum; whole infant marmoset body (1–8 weeks of incubation with pre-conjugated 2° Fab-1° Ab)	various chemical dyes (DAPI, SYTO 16, SYTOX Green, RedDot2 Far-Red nuclear stain, NeuroTrace 640/660, Deep-Red fluorescent Nissl stain, BOBO-1 iodide, propidium iodide, eosin)	no	yes	requires careful handling of fragile tissue with spoon (i.e., avoid tweezers)
	eFLASH ²⁴	tuning Ab-Ag binding affinity with NaDC and pH	whole adult mouse brain (1 day)	endogenously expressed fluorescent proteins; chemical/protein probes (SYTO 16, lectin)	yes	no	equipment dependent; max. scale shown combined with SE, P3PE is not widely available
	ThICK ¹⁸	heat inhibition of Ab-Ag binding, permitted by thermostabilized Abs termed SPEARs	whole adult mouse brain (3 days of incubation with SPEARs at 55°C)	endogenously expressed fluorescent proteins	no	no	requires optimization of Ab dilution, P3PE is not widely available

1° Ab, primary antibody; 2° Fab, secondary fragment antigen-binding region; Ab, antibody; Ag, antigen; CUBIC-HV, clear, unobstructed brain imaging cocktails and computational analysis-HistoVision; ELAST, entangled link-augmented stretchable tissue-hydrogel; EdU, 5-Ethynyl-2'-deoxyuridine; SHANEL, small-micelle-mediated human organ efficient clearing and labeling; SHIELD, stabilization under harsh conditions via intramolecular epoxide linkages to prevent degradation; SPEAR, synergistically protected polyepoxide-crosslinked Fab-complexed antibody reagents; SWITCH, system-wide control of interaction time and kinetics of chemicals; TRITC, Tetramethylrhodamine isothiocyanate; ThICK, thermo-immunohistochemistry with optimized kinetics; eFLASH, electrophoretically driven fast labeling using affinity sweeping in hydrogel; iDISCO, immunolabeling-enabled three-dimensional imaging of solvent-cleared organs; uDISCO, ultimate DISCO; vDISCO, nanobody(VHH)-boosted 3D imaging of solvent-cleared organs.

pH

The pH dependence of Ag binding capability varies across Abs. Unless specifically engineered, most Abs require or are designed to function under a relatively neutral pH (typically between pH 6.5 and 8.5). At extreme pH for extended durations, conformational changes induced may be irreversible.²⁷ However, most Abs can be exposed to acids and bases for reasonable lengths of time and still retain their full Ag-binding capability. pH is therefore a controllable environmental parameter to fine-tune Ab-Ag binding affinity. When manipulating K_{eq} by ionic strength and pH, one caveat is that one should also consider the effects of possible tissue shrinkage or expansion given changes in the buffer composition, which may affect immunostaining by altering the diffusion distance.¹⁷

Detergents

Ab-Ag binding can be hindered by detergents. Generally, ionic detergents (e.g., sodium deoxycholate [NaDC], sodium dodecyl sulfate [SDS]) inhibit Ab-Ag binding more strongly, while non-ionic detergents (e.g., Triton X-100, Tween 80) have relatively mild effects.^{28,29} However, the structural and physicochemical determinants of each detergent's ability to modulate Ab-Ag binding are highly complex and remain poorly understood because this can occur either by micellar coating of the Ab-Ag interaction interface, denaturation of Ab domains (especially the C_{H2} domain),³⁰ disruption of water molecules involved in the Ab-Ag non-covalent bonds, or a combination of these effects. The effect of detergents on proteins is further modulated by the ionic strength and pH of the solution, which also alters the critical micelle concentration (CMC), aggregation number, as well as micelle size and properties of detergents.

Despite the complex nature, the empirically determined effects of detergents on Ab-Ag interaction can be practically very useful. Notably, it was found that NaDC reduces Ab-Ag binding at sufficiently high concentrations and offers the convenience of tunable inhibition because the effect is concentration dependent.²⁸ SDS is a much stronger Ab-Ag interaction inhibitor than NaDC and other non-ionic detergents. Interestingly, inhibition of the Ab-Ag reaction by SDS can be weakened in the presence of another non-ionic detergent,³¹ highlighting the complex interactions between individual detergent molecules, mixed micelles, Abs, and Ags.

FACTORS DETERMINING AB DIFFUSIVE AND ADVECTIVE TRANSPORT

Enhancing Ab diffusivity is a universally adopted strategy in standard immunostaining, achieved principally by tissue permeabilization. When scaling up to the immunolabeling at millimeter or even centimeter depths, the intrinsic physicochemical properties of Abs and other factors that determine their diffusive and advective transport need to be considered.

Diffusion distance and timescale

To allow more quantitative considerations regarding the distances Abs can travel within a given time, we may first focus on a pure diffusive process, described by

$$\frac{\partial [Ab_r]}{\partial t} = D_{eff} \nabla^2 [Ab_r]. \quad (\text{Equation 5})$$

It can be shown that, for a 3D diffusion process described by Equation 5 (interested readers may refer to Berg³² for the detailed derivation), given a point source at time zero, the mean-squared distance from the source (denoted by $\langle ||r||^2 \rangle$) traveled by a molecule with a random walk after a time interval (Δt) is given by

$$\langle ||r||^2 \rangle = 6D_{eff} \Delta t, \quad (\text{Equation 6})$$

which is equivalent to

$$\Delta t = \frac{\langle ||r||^2 \rangle}{6D_{eff}}. \quad (\text{Equation 7})$$

We can thus infer that, on average, in the absence of Ab depletion or advection, the time it takes for an Ab molecule to reach a given spatial location in a tissue sample via diffusion scales quadratically with the distance from the surface and inversely with Ab diffusivity in the tissue. Also note that, for a point source with Ab concentration $[Ab_r]$ and spherical vicinity of a given small radius $\sim \sqrt{\langle ||r||^2 \rangle}$, $[Ab_r]/\Delta t$ gives the Ab diffusive transport rate as the inverse of the time Δt it takes for Abs to diffuse to a mean-squared distance of $\langle ||r||^2 \rangle$ from the source, scaled by the concentration $[Ab_r]$.

With the reaction term but without advective transport, and provided that there is negligible Ab-Ag dissociation (e.g., for high-affinity Abs under conditions favoring exothermic reactions), the equation for a reaction-diffusion process is given by

$$\frac{\partial [Ab_r]}{\partial t} = -k_a [Ab_r][Ag] + D_{eff} \nabla^2 [Ab_r], \quad (\text{Equation 8})$$

for which it would be useful to consider the ratio of Ab-Ag reaction rate to Ab diffusive transport rate, which defines the Damköhler number (Da); i.e.,

$$\begin{aligned} Da &= \frac{k_a [Ab_r][Ag]}{[Ab_r]/\Delta t} \\ &= \frac{k_a [Ag] \langle ||r||^2 \rangle}{6D_{eff}} \end{aligned} \quad (\text{Equation 9})$$

Da is a critical determinant of Ab movements in a reaction-diffusion process, which can be equivalently considered as the ratio of the Ab diffusive transport timescale to the Ab-Ag reaction timescale. For a large Da, the process is diffusion limited (e.g., dense accessible Ag target, under favorable binding conditions or low Ab diffusivity) and hinders Ab penetration. With a small Da, the process is reaction limited (e.g., when there are very sparse Ags along the transport path, Ag-Ab binding is not favored by the physicochemical environment, or Ab diffusivity is high) and facilitates Ab transport. Ideally, simultaneously decreasing k_a and increasing D_{eff} would be the most effective way to enhance deep probe penetration.

Tissue permeability

Naturally, tissue components, such as cell membranes and the ECM, form barriers to Ab movement. Tissue permeabilization is required for standard IHC to enable Ags to become accessible by Abs. This is commonly accomplished using organic solvents or detergents. Quantitatively, we may consider a tissue a porous

medium and model the effect of diffusion hindrance by a scaling factor $\gamma < 1$ as follows:

$$D_{\text{eff}} = \gamma D, \quad (\text{Equation 10})$$

where D is the molecular diffusivity or diffusion coefficient in the same immersion fluid medium without tissues. Permeabilization is therefore, in this regard, a measure to bring γ closer to 1. To scale up permeabilization to the whole-tissue or organ level, detergent properties, such as the CMC, aggregation number, micelle size, and interactions with other molecules, are additional crucial factors to consider because their mobility in tissues is also governed by the RDA model. Moreover, their effects on Ab-Ag binding and fluorescence signal preservation also critically determine the applicability in IHC. Note, however, that Ag accessibility may also be enhanced with permeabilization. This is equivalent to an increase in $[Ag]$ in the numerator of Da (Equation 9). The penetration depth therefore does not necessarily simply scale directly with the associated D_{eff} increase.

Ab properties and temperature

The classical model relating the properties of a molecule to its diffusivity in a fluid medium is the Einstein relation, stating that:

$$D = \mu k_B T, \quad (\text{Equation 11})$$

where μ is the mobility of the molecule, k_B is the Boltzmann constant, and T is the absolute temperature. For an Ab, within the feasible range of heating in immunostaining, the increase in temperature can modestly enhance D (or D_{eff}). For example, one would only expect a roughly 10% diffusivity increase with a temperature increase from 20°C to 50°C.

In the Stokes-Einstein model, the mobility of a molecule is given by

$$\mu = \frac{1}{6\pi R_H \eta}, \quad (\text{Equation 12})$$

where R_H is the hydrodynamic radius of the molecule, and η is the dynamic viscosity of the fluid medium. Note that μ is inversely proportional to R_H , which, in turn, directly scales with molecular size. Because single-domain heavy-chain-only Abs, or nanobodies, are only ~ 15 kDa (i.e., one-tenth the size of typical full-sized Abs [~ 150 kDa]), they exhibit substantially better mobility and diffusivity than Abs. In a study that performed direct experimental measurements, it was reported that the diffusivity of immunoglobulin G (IgG) in water (D_{water}) is $\sim 1/3$ of that of nanobodies, and the D_{eff} in hydrogel-embedded and permeabilized mouse brain tissue sections is around one-fourth of D_{water} .³³ In contrast, nanobodies measured exhibited more than 10 times higher D_{eff} than immunoglobulin G in the tissue sections and nearly identical diffusivity values in hydrogel and in water. The use of nanobodies is therefore a good strategy to enhance probe penetration with two caveats: (1) validated nanobodies are generally far less available for many Ag targets, and (2) dim signals are frequently observed because of a lack of amplification unless used as secondary probes targeting primary Abs.

Because Abs are typically charged (unless the pH is exactly at their isoelectric points), we may further consider the electrical mobility (or electromobility) μ_q for an Ab with charge q , given as

$$\begin{aligned} \mu_q &= \mu q \\ &= \frac{q}{6\pi R_H \eta}. \end{aligned} \quad (\text{Equation 13})$$

This is an important quantity because it relates to the diffusivity and determines the velocity field \mathbf{v} of Ab advective movement subject to an externally applied electric field \mathbf{E} (which could be constant or vary with space and time), with \mathbf{v} given by

$$\mathbf{v} = \mu_q \mathbf{E} \quad (\text{Equation 14})$$

Additional considerations of Ab movement and reaction time scales

In most cases, the substantial difference in the timescales of Ab movement across tissue (hours to weeks) and Ab-Ag reaction (sub-seconds) needs to be considered. This discrepancy implies that, unless the accelerated Ab movement can catch up with the reaction timescale, Abs are still prone to depletion by densely expressed Ags near the tissue surface, resulting in a rimming pattern of staining. Ultimately, the main goal of deep immunostaining approaches is to achieve the following condition:

$$t_{\text{transport}}(\mathbf{r}, D_{\text{eff}}, F) \leq t_{\text{reaction}}(K_{\text{eq}}), \quad (\text{Equation 15})$$

where $t_{\text{transport}}$ is the transport timescale for reaching the deepest spatial location \mathbf{r} in tissue, F denotes the net effect of all externally applied forces (which depends on Ab properties; e.g., μ_q for electric force [Equation 13], mass for mechanical force), and t_{reaction} is the reaction timescale. Achieving this condition amounts to the shortening of $t_{\text{transport}}$ and lengthening of t_{reaction} and can be considered a generalization of Da (Equation 9) minimization. It applies to all approaches that facilitate Ab transport (e.g., via enhancing diffusion, modulating Ab-Ag binding modulation, and creating advective movements) at the tissue-size scale.

DEEP IMMUNOLABELING: TECHNICAL APPROACHES

A pipeline for deep immunostaining typically consists of several modules: (1) sample fixation, (2) optional tissue pre-treatment (e.g., hydrogel embedding, dehydration), (3) permeabilization, and (4) immunostaining. In practice, the majority of deep IHC methods are coupled with optical clearing, which typically adds an extra module of (5) refractive index matching, followed by (6) volumetric imaging, although this is not strictly necessary when tomography by serial sectioning is employed. The variety of deep IHC approaches stems from the combination and modification of each of these modules. These modules need not be performed in separate procedures. For example, tissue delipidation may take place during incubation in staining buffers containing detergents.

Existing deep immunolabeling approaches can be broadly classified into two categories based on their main principle adopted to enhance Ab penetration (Figure 2; Table 1): (1) modulation of Ab-Ag binding, and (2) facilitation of Ab diffusion and/or advective transport. The shared principle behind techniques based on modulation of Ab-Ag interaction is that by temporarily inhibiting Ab-Ag binding, less Ab depletion occurs and more

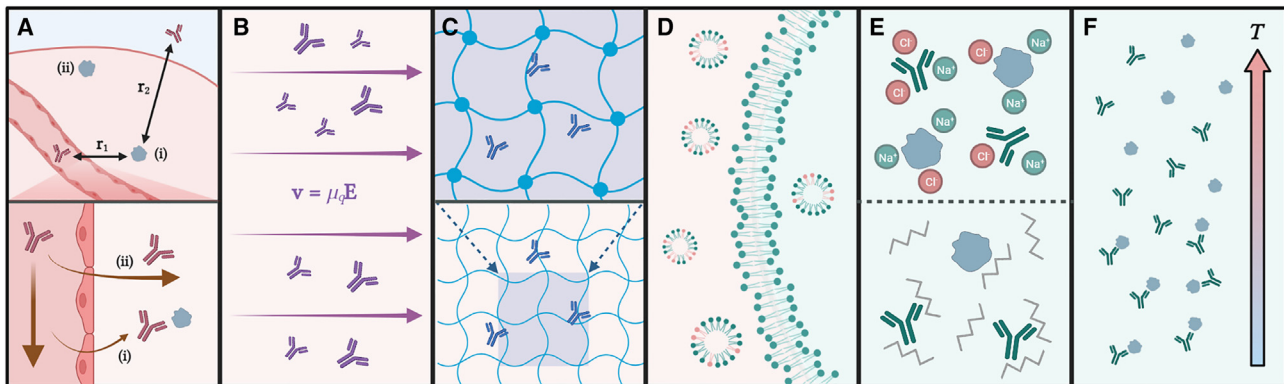


Figure 2. A graphical summary of deep immunostaining technical approaches

(A) Infusion of Abs into the tissue via the intact vasculature as in vDISCO, which (i) decreases the diffusion distance (r_1 from the nearest vessel $< r_2$ from the tissue surface) and (ii) allows advective transport across vessel walls driven by mechanical pressure gradients to assist Abs to reach deep-tissue Ags.
 (B) Creation of advection via an electric field utilizing the electromobility of Abs as in SE. The representation of the electric field (purple) here is simplified.
 (C) Transformation of tissue into a hydrogel, which allows shrinkage in size to reduce diffusion distance, as in ELAST.
 (D) Optimized permeabilization of the cell membrane to enhance Ab penetration, as in iDISCO and SHANEL, by formation of lipid micelles. Green, membrane lipids; red, detergents.
 (E) Non-covalent interference of Ab-Ag interactions by manipulation of ionic strength and/or pH (top panel, using NaCl as an example), as in eFLASH, and by addition of detergents (bottom panel), as in SWITCH. Gray, detergents.
 (F) Thermal inhibition utilizing the exothermic nature of Ab-Ag reaction, as in ThICK with SPEARs.
 The figure was created with BioRender.

mobile, Abs are available to diffuse deeper into tissue. This has been accomplished in different ways, using detergents (e.g., SDS, NaDC), non-specific denaturants (e.g., urea, Quadrol), tuning pH, heating, or combinations of these (Figures 2D–2F). On the other hand, Ab movement can be enhanced by tissue permeabilization, reducing the distance to reach Ag targets, and/or use of externally applied force fields to create advective transport (Figures 2A–2C).

Suppression of Ab- Ag binding by non-covalent modifications

SWITCH makes use of the strong Ab-Ag binding inhibition property of SDS, which is also a tissue-permeabilizing agent.²³ In the SWITCH protocol, the tissue sample is first immersed in and equilibrated with a solution containing 0.5 mM or more SDS (up to 10 mM, the CMC of SDS). Abs are then added and diffuse into tissue over hours to days, depending on tissue size, before the sample is switched to an incubation solution with just Triton X-100 in PBS to allow Ag binding. CUBIC-HistoVision (CUBIC-HV) combines several approaches, including (1) optimizing Ab concentration, detergent (10% [v/v] Triton X-100), ionic strength (at 200 mM NaCl), chemical additive composition (urea and Quadrol) and their concentrations; (2) adopting a higher incubation temperature (room temperature or above); and (3) use of one-step labeling with secondary Fab-conjugated primary Abs to eliminate the need for repeated probe penetration.¹⁷ Importantly, use of urea and Quadrol in CUBIC-HV enhances Ab penetration depth and homogeneity, likely mainly via their inhibitory effect on Ab-Ag binding (on top of tissue permeabilization effects). Likewise, in eFLASH, gradual tuning of pH from basic (~9.7) to more neutral (~7.5) and NaDC concentration from high (~1% [w/v]) to low (~0.5% [w/v]) during Ab incubation turns the Ab-

Ag reaction environment from unfavorable to favorable (while enhancing Ab movements with stochastic electrotransport [SE], discussed in a later section).²⁴ Millimeter-thick mouse brain tissue can be uniformly immunostained with SWITCH, whereas CUBIC-HV and eFLASH demonstrated thorough immunolabeling of intact mouse whole brains. While allowing high-quality multiplexed staining with up to four Abs, CUBIC-HV is relatively time consuming, requiring weeks to months to complete.

Suppression of Ab- Ag binding by elevated temperature

ThICK staining uses transient heating to 55°C during Ab incubation to inhibit Ab-Ag binding with simultaneous enhancement of Ab diffusivity and achieves whole-mouse-brain immunolabeling quickly and completely (with a small contribution by increased diffusivity during heating)¹⁸ (Figure 2F). Similar to CUBIC-HV and eFLASH, a one-step approach with Fab-conjugated primary Abs is adopted. Such a thermally facilitated method is possible only with additional intramolecular crosslinking of Fab-conjugated Abs using polyglycerol-3-polyglycidyl ether (P3PE), which effectively prevents heat and chemical denaturation of the modified Abs (termed SPEARs). Compared with other methods, ThICK staining with SPEARs is much quicker (e.g., within 72 h with ThICK vs. 1–8 weeks with CUBIC-HV for a whole mouse brain) and does not require dedicated equipment. The approach is also readily generalizable to many off-the-shelf primary Abs and has been tested on some nanobodies. However, the lower signal-to-background ratios because of higher staining backgrounds with ThICK staining for some Ag targets still warrant further improvements. In addition, like several other methods, ThICK staining has yet to be optimized for minimization of the rimming effect and compatibility with other molecular labeling techniques, such as fluorescence *in situ* hybridization.

Facilitating diffusion by enhancing tissue permeability Solvent-based permeabilization

In solvent-based clearing methods, suitable solvents (e.g., dichloromethane or chloroform) are used to extract and remove membrane lipids, achieving adequate tissue permeabilization. Because these solvents are water immiscible, these methods require prior graded dehydration with water-miscible solvents (e.g., methanol in iDISCO³⁴ and tert-butanol in uDISCO³⁵). These methods have been used to stain tissues ranging from millimeter-thick mouse brain slices to intact whole mouse embryos.

Detergent-based permeabilization

Detergents insert into cell membrane lipids via their hydrophobic moieties (e.g., long non-polar tails) and extract membrane lipids via formation of soluble mixed micelles, permeabilizing the tissue. While detergents such as SDS and Triton X-100 are commonly used in standard immunostaining, their structures lead to formation of large micelles with low diffusivity, limiting their permeabilization capability of large tissue blocks. To overcome such a limitation, SHANEL makes use of CHAPS (3-[(3-cholamidopropyl) dimethylammonio]-1-propanesulfonate),²⁰ a cholanoate derivative with an ellipsoidal molecular geometry that directly leads to a lower aggregation number and, hence, smaller micelles compared with SDS and Triton X-100.³⁶ In a head-to-head comparison, 10% (w/v) CHAPS can permeabilize paraformaldehyde (PFA)-fixed pig pancreatic tissues much better than 200 mM SDS or 10% (w/v) Triton X-100. In addition to permeabilization, SHANEL also combines loosening of the ECM with acetic acid (0.5 M) and guanidine hydrochloride (4 M).²⁰ The technique has been shown to be compatible with various Abs and chemical dyes (e.g., TO-PRO-3 and Methoxy-X04) while enabling thorough immunostaining and microscopic imaging of up to 1.5-cm-thick human brain tissue.

Other chemicals and methods

Alternatively, tissues can be permeabilized with other chemicals, such as urea and Quadrol. These have been used in several clearing methods, such as Scale,³⁷ CUBIC,³⁸ and CUBIC-HV, where tissues are chemically delipidated, hyperhydrated, and cleared prior to immunolabeling. Thus far, use of the various chemicals has been based on empirical testing, and the exact mechanisms by which they may enhance probe diffusion in tissues often remains unclear. It is possible that a high concentration of urea hyperhydrates tissue by disturbing protein interactions and relaxing protein scaffolds, thereby increasing tissue osmotic pressure to promote diffusion of molecules into deeper tissue regions. Alternatively, residual urea may also facilitate Ab penetration by preventing their reaction with tissue Ags.

While these methods focus on disrupting the cell membrane barrier, controlled proteolysis has also been explored. For example, tissue digestion with Proteinase K in expansion microscopy facilitates Ab penetration of expanded tissue-hydrogel structures while preserving the epitopes.³⁹ In CUBIC-HV, an optional step of limited ECM digestion with collagenase P or hyaluronidase also improves probe penetration without disrupting endogenous fluorescent protein signals.¹⁷

Facilitating diffusion via reduction of diffusion distance and mechanical approaches

Because the timescale to reach a target location within a tissue via diffusion scales quadratically with the depth, reducing the physical distance from the tissue surface or Ab source can efficiently improve probe penetration. Taking advantage of the chemically tunable mechanical properties of tissue-hydrogel structures, ELAST takes a creative approach to reduce diffusion distance.²² Converting tissues into thermochemically and mechanically stable tissue-hydrogel hybrids has been very successful because of flexibility in modifying tissue physical size, as in use of sodium acrylate in expansion microscopy (e.g., magnified analysis of the proteome [MAP]).^{39,40} ELAST uses very high acrylamide to initiator and crosslinker concentration ratios to form a highly elastic tissue-hydrogel structure. The modified tissue structure can then be reversibly and transiently stretched or compressed during immunolabeling, effectively shortening the distances for Abs to diffuse to reach deep regions (Figure 2C). ELAST was successfully applied to up to 5-mm-thick human brain tissue slices, achieving complete immunolabeling within 1 day.²²

Another approach based on reducing diffusion distance is vDISCO, which uses transcardial perfusion of nanobodies to achieve whole-organ and even whole-body immunolabeling.²¹ In vDISCO, after PFA perfusion and decolorization steps, high-pressure (160–230 mmHg) transcardial perfusion of permeabilization and staining solutions is performed. For most organs, the average distance between a given cell and the nearest capillary is only tens of micrometers.⁴¹ Therefore, apart from directly forcing labeling molecules into deep tissue regions, the strategy also greatly reduces the traveling distance for the more diffusive nanobodies (relative to full-sized Abs) to reach target cells (Figure 2A). vDISCO is especially optimal for labeling whole-organ tissues with intact vasculature. However, only nanobodies targeting fluorescent proteins and some chemical dyes (e.g., propidium iodide) have been tested and validated with the method thus far. vDISCO also consumes a large amount of nanobodies, requiring 5–8 μg of nanobodies for labeling a mouse brain and ~ 25 –40 μg nanobodies for staining a whole mouse body.²¹

Creation of advective transport with electric fields

Because Abs are often charged, externally applied electric fields can drive advection of Abs and accelerate immunolabeling (cf. Equations 1, 3, 13, and 14; Figure 2B). Because tissues contain other charged molecules, general electrophoresis may disrupt target biomolecules and cause tissue damage. SE, based on use of a rotating electric field, was thus developed to accelerate dispersion of Abs in tissue samples without damaging other charged molecules.¹⁶ SE selectively drives advection of highly charged mobile molecules (e.g., Abs) while preventing excessive movements of molecules with lower electrophoretic mobility (i.e., other tissue-endogenous molecules, including Ags). Combined with affinity sweeping (as in eFLASH) and improved tissue stability with SHIELD (a hydrogel-based tissue preservation method),⁴² deep probe penetration throughout a whole mouse brain can be achieved within a day. The only drawback is the need for specialized equipment for different-size samples.

QUALITY CONTROL AND BENCHMARKING FOR DEEP IMMUNOLABELING

Metrics for quantitative benchmarking of deep immunostaining methodologies

While each of the methods has been cleverly designed, comprehensive and stringent head-to-head comparisons are required to evaluate the relative performance of the different approaches in different applications. This would provide crucial information for researchers to choose the optimal method for addressing their biological questions of interest. For fair and quantitative evaluations of existing and newly developed methods, three metrics are of particular interest: penetration depth of probes, staining homogeneity, and staining specificity.

Penetration depth of probes

A sufficient penetration depth is a prerequisite for examining the homogeneity and specificity of staining in large tissues. Upon staining, signal intensities of voxels with labeled markers increase, and a subset of them exceeds the detection threshold of the optical system used. Depending on the experimental objective, suprathreshold voxels may be grouped together as units (e.g., segmented as cells). The penetration depths of probes can then be defined as the maximal value of the shortest distances between the suprathreshold voxel units and the tissue surface.

Staining homogeneity

Quantitative 3D IHC for many tissue markers necessitates homogeneous staining. Staining homogeneity is determined by the extent of equal Ab accessibility of Ags across the tissue. One or more tissue markers with uniform distribution across depths should be chosen for IHC, and a high staining homogeneity is demonstrated when maximal signal homogeneity (or minimal signal variability) versus depth is obtained. Quantification can be achieved by examining marker-associated voxel signal intensity versus distance from the nearest tissue surface, followed by appropriate curve-fitting and parameter extraction. In general, for the rimming effect commonly observed in deep IHC, empirical fitting with an exponential decay function would be a reasonable choice. Staining homogeneity may then be quantified using one or more fitted parameters (e.g., the decay distance constant of a fitted exponential curve).

Staining specificity

Many Ags have heterogeneous spatial distributions, and authentic results of immunolabeling should faithfully reveal their characteristic patterns in tissues. Staining specificity against a given Ag or marker can thus be defined as the resemblance of the staining pattern obtained via deep IHC methods to the ground-truth distribution in thin sections. The experimental approach and quantifications required to obtain such information, along with penetration depth and staining homogeneity, are outlined in the next section.

Apart from these metrics, additional considerations, such as the range of compatible Abs, signal-to-noise ratio, multiplexing capability, and compatibility with other probe labeling modalities (e.g., concurrent RNA fluorescent *in situ* hybridization, chemical dye labeling, or lipophilic dye tracing), are also important factors determining the suitability of a deep IHC method for a specific biological question.

Marker selection and a stringent benchmarking scheme

The aforementioned criteria for assessing deep IHC methodologies depend on the chosen tissue Ags, but it would be impractical to benchmark each method with all possible markers. A wise strategy for marker selection is therefore needed, potentially by categorizing tissue markers according to their expected ideal 3D immunolabeling effects, requiring inclusion of representative markers under each proposed category to be demonstrated in a standardized test. We propose the following principles of selecting appropriate markers for benchmarking deep IHC: (1) markers unambiguously expressed by readily discernible cells (e.g., parvalbumin [PV]-positive cells in brain tissue), to provide readily identifiable focal points for their segmentation and IHC intensity-penetration distance analysis; (2) densely expressed markers (e.g., neurofilament [NF] and NeuN in brain tissue) that magnify the differences in penetration depth and staining homogeneity between different deep IHC methods because a high concentration of Ags promotes Ab depletion and accentuates the rimming effect; (3) markers with known characteristic spatial arrangements, such as a patchy or layered spatial pattern along the surface-center axis (e.g., cortical layer-specific neuronal markers); as well as (4) markers with isoforms/similar structures to facilitate assessment of staining specificity. A similar approach for marker selection can be adopted for different organ tissues.

After selecting the marker set, we suggest adopting a stringent two-step head-to-head benchmarking scheme as adopted by several studies^{18,43} (Figure 3), which is readily implementable in standard laboratories. The first part involves staining of tissue with the methods under evaluation (termed bulk staining), while the second part involves cutting the bulk-stained tissue at specific locations and counter-staining the same marker with a different probe set under conventional IHC conditions (termed cut staining). Intra- and inter-methodological benchmarking of performance in terms of penetration depth, staining homogeneity, and staining specificity are equally important, where intra-methodological benchmarking refers to optimization of staining conditions for a given method. In cut staining, Abs can directly reach the cut surface to provide a ground truth for comparison with signals obtained with bulk staining. Exposure of the cut surface also allows unobscured optical imaging across bulk staining depths, alleviating any potential signal dampening because of optical aberrations and attenuations that can occur even with adequate optical clearing. This would facilitate more accurate quantification of staining depth and homogeneity and validation of immunolabeling specificity. Tissue expansion or shrinkage factors should also be considered during quantification of staining penetration distances. For an ideal deep IHC method, the bulk staining signals should strongly correlate with that of cut staining across all penetration depths. This applies to markers under all different categories.

Note that the suggested general scheme should be flexibly adopted to different tissue types, markers of interest, and knowledge of the tissue characteristics and chosen methodology. For example, a direct comparison of endogenous fluorescent proteins with their deep IHC signal would also be valid. Staining of vasculature, being a dense, almost universal structure in biological tissues (except, e.g., cartilage, cornea), provides easy

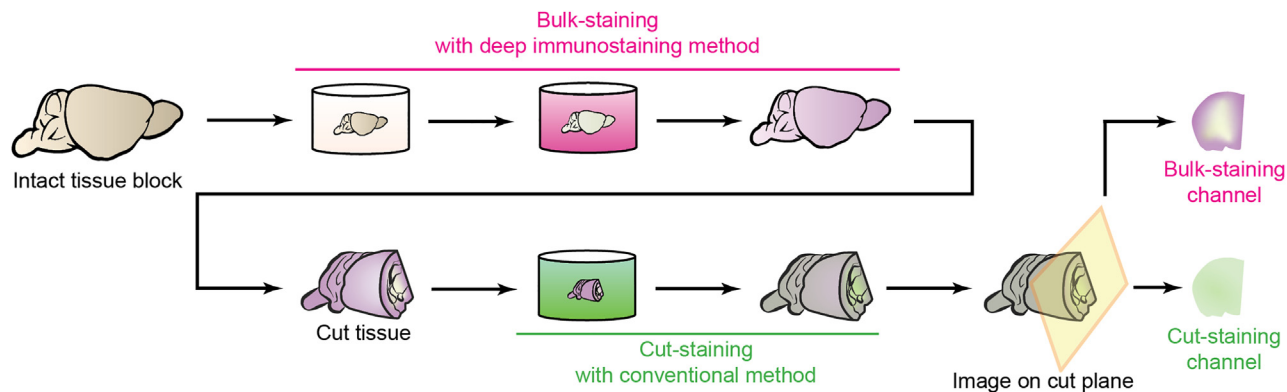


Figure 3. A standardized benchmarking scheme for deep IHC

In this example, an appropriate marker in a mouse hemibrain is first stained with the deep IHC method of interest (magenta, bulk staining), followed by cutting the tissue and re-staining in standard immunostaining buffer (e.g., PBS with 0.1% Tween 20) for the same marker with a spectrally non-overlapping fluorophore (green, cut staining). The tissue is then imaged on the cut plane, where cross-comparison of both channels will reveal how well the deep IHC method reproduces the expected pattern in section-based conventional IHC. In this illustrated example, the deep immunostaining method has limited penetration, causing a rim of stronger magenta signal near the tissue surface than at its core.

Adapted from Lai et al.¹⁸

choices of markers for benchmarking. However, caution should be exercised during data analysis because vasculature frequently contains clumped Abs and autofluorescent blood cells and elastin, which should be distinguished from true IHC signals. In addition, the spatial distribution of certain markers may vary between different loci within the organ and the pathophysiological state of the tissue; hence, their staining patterns should first be established in the literature or traditional tissue sections. Finally, some methods may modify the mechanical properties of the tissues, such as those that have undergone hydrogel embedding and extensive tissue delipidation, making a clean cut technically challenging.

FUTURE STRATEGIES AND UNADDRESSED ISSUES

Approaches based on unexplored principles

Some principles remain to be tested for lengthening of the Ab-Ag reaction and shortening of probe transport timescales. For instance, during the Ab transport process, temporarily denaturing tissue Ags or their epitopes could lower the effective concentration of available Ags (i.e., reducing accessible Ags in the reaction term $-k_a[Ab_i][Ag]$ in Equations 2 and 3 to decrease Ab depletion). This can potentially be achieved by thermal and chemical methods, followed by renaturation of the Ags after the Abs have diffused homogeneously into the tissue. To speed up labeling probe transport, methods that maximize the mobility μ of probes by minimizing the denominator of the expression for μ (e.g., minimizing the hydrodynamic radius R_H or the viscosity of the medium η in Equation 12) could be tested. These may be accomplished by use of a *de novo*-designed, Ag-specific mini-protein binder that would have a high diffusivity because of a small hydrodynamic radius and by use of specific solutes that alter η by weakening the intermolecular interactions between the solvent and/or probe molecules. In addition, whether certain chemicals (e.g., organic solvents, chaotropes) may be used to modulate Ab-Ag binding reversibly while simultaneously weak-

ening Ab interactions with tissue and immersing medium molecules to facilitate Ab transport has also yet to be further explored.

Challenges in multiplexed deep immunolabeling

To address many research questions regarding the structural organization and cellular interactions in a biological system, it is necessary to profile a relatively large panel of proteins. Considering that, for 3D IHC, (1) tissue processing time scales quadratically with the diffusion scale and (2) to target a panel of n Ag targets, each round of staining and stripping further lengthens the time by $2n$ -fold, multiplexed staining in each round is much desired. With respect to Ab utilization, the traditional approach of targeting primary Abs with species-specific fluorescent secondary Abs or nanobodies is economically desirable. However, co-use of primary Abs for targeting different Ags from the same host causes secondary Abs to cross react. The need for a host-orthogonal Ab panel thus largely limits the multiplexing capability of the classical approach. Although blocking strategies exist, most are inefficient and time consuming, especially at a large volumetric scale. While use of fluorophore-conjugated primary Abs is a trivial solution to the problem, such a strategy is relatively inflexible, requires extra steps of synthesis, and can affect staining specificity. To this end, various approaches for multiplexed immunolabeling have been developed, most of which require conjugation of primary Abs to readout moieties (e.g., DNA barcodes).⁴⁴ However, given the typically low yields of the chemical synthesis procedures involved, inefficient probe utilization and the associated increased costs are still unaddressed issues with the existing methods. Substantial further efforts are therefore required to advance the multiplexing capability of deep immunostaining.

COMPATIBILITY WITH OTHER PROBE LABELING MODALITIES

IHC and other probe labeling techniques can provide complementary information crucial for interrogating cellular processes.

Further developments of deep IHC methods should therefore also attempt to maximize the inter-compatibility of different labeling modalities. To highlight a few, these include compatibility with (1) spatial RNA and epigenetic profiling; (2) various chemical dyes, such as nucleic acid stains and lipophilic tracers; and (3) small peptide and protein binders.

Spatial RNA and epigenetic profiling

The concentration of RNA transcripts and that of the translated proteins often have a nonlinear relationship because of many factors, including (1) temporal discrepancy, because protein synthesis lags behind mRNA level fluctuations; (2) spatial discrepancy, where protein transport processes spatially dissociate proteins from their parent transcripts; (3) translational rate modulations by various mechanisms (e.g., RNA modifications and non-coding RNA regulation); and (4) post-translational modifications, especially those that affect protein stability and turnover.⁴⁵ These all add to the complexity of gene expression, which is also regulated at the levels of histone and DNA epigenetic modifications. Combining deep IHC with 3D spatial transcriptomic and epigenomic profiling methods would enable an unprecedented understanding of the spatiotemporal control of gene expression regulation and the functional consequences. Simultaneous profiling of multiple biomolecular modalities is therefore of great interest in physiological states (e.g., compartment-specific local mRNA translation in neuronal dendrites, somata, and axons⁴⁶), and pathological states (e.g., transcriptional changes in the vicinity of protein aggregates in neurodegenerative diseases⁴⁷). However, the tissue-processing steps in many current deep IHC methods may result in significant loss of nucleic acids, especially the more fragile RNAs. Obtaining accurate results of 3D protein and transcriptomic/epigenomic profiling thus remains a major challenge.

Chemical dyes

Small-molecule probes serve as a robust labeling modality that complements deep IHC protein staining, such as DNA minor-groove binders (e.g., DAPI) for tissue orientation via locating cell nuclei and lipophilic dyes for neuronal fiber tracing in post-mortem brain tissues. However, the performance of these probes may be compromised by tissue processing in deep IHC. For instance, use of charged additives may interfere with nucleic acid labeling, while application of detergents in tissue permeabilization may result in delipidation and strip off lipid-specific dyes. Hence, depending on the specific experimental goal, the choice of deep IHC methods may be additionally limited by the compatibility with specific chemical dyes.

Peptide and protein probes

Experiments utilizing deep IHC are not only limited by the compatibility of existing methods with specific Abs but also by the availability of high-quality Abs for specific Ag targets. Currently, there exists a considerable pool of Ags that lack validated Abs for immunostaining. The use of non-validated Abs may lead to irreproducible and even incorrect results. One potential way to help tackle this problem is to extend the scope of probes from Abs to general protein binders to which most principles for achieving deep IHC apply equally. Recent ad-

vancements in *de novo* protein design could, in principle, allow researchers worldwide,^{48,49} instead of only commercial suppliers, to contribute to the field by designing target-specific binder proteins for Ags lacking validated Abs. This can be foreseen to further accelerate the progress in 3D histology.

CONCLUDING REMARKS

Just as computed tomography and magnetic resonance imaging revolutionized modern medicine by providing organ details unattainable with plain radiography, 3D profiling of biomolecules is poised to greatly advance our knowledge of the anatomical and functional organization of whole tissues and organisms by enabling their holistic characterization. A field still in its infancy, substantial technical developments are required to overcome existing hurdles that hinder wider adoption of deep IHC by the research and clinical communities. By formulating the problem of achieving deep, homogeneous immunolabeling in a systematic manner, we hope that the principles, methods, benchmarking approaches, and future directions outlined in this review will enable researchers to devise their experimental designs. Ease of use at reasonable cost, sufficient labeling homogeneity across tissue depth for quantitative analysis, scalability of multiplexing capability, and multimodal profiling compatibility are among the most important desired attributes yet to be achieved in the field. Although some of the techniques developed for deep IHC are generalizable, simultaneous profiling of multiple biomolecule types in large-volume tissues necessitates more innovative approaches to ensure that the faithful readouts are reflective of that in the native biological context. These will pave the way toward actualizing the full potential of tissue- and organism-wide 3D multi-omics.

ACKNOWLEDGMENTS

Work in the Lai and Ko labs is supported by a Croucher Innovation Award (CIA20CU01) from the Croucher Foundation; a Faculty Innovation Award (FIA2020/B/01) from the Faculty of Medicine, CUHK; the Midstream Research Programme for Universities (MRP/048/20) of the Innovation and Technology Council of Hong Kong; the General Research Fund (14100122), the Collaborative Research Fund (C6027-19GF and C7074-21GF), and the Area of Excellence Scheme (AoE/M-604/16) of the Research Grants Council, University Grants Committee of Hong Kong; the Excellent Young Scientists Fund (Hong Kong and Macau) (82122001) from the National Natural Science Foundation of China; the Margaret K.L. Cheung Research Centre for Parkinsonism Management, Faculty of Medicine, CUHK; and Lo's Family Charity Fund Limited. The graphical abstract was in part produced in [BioRender](#).

DECLARATION OF INTERESTS

The authors declare no competing interests.

REFERENCES

1. Delesse, M. (1847). Procédé mécanique pour déterminer la composition des roches. *CR Acad. Sci. Paris* 25, 544–545.
2. Spalteholz, W. (1911). Über das Durchsichtigmachen von menschlichen und tierischen Präparaten: nebst Anhang, Über Knochenfärbung (S. Hirzel).

3. Lai, H.M., Ng, W.L., Gentleman, S.M., and Wu, W. (2017). Chemical probes for visualizing intact animal and human brain tissue. *Cell Chem. Biol.* **24**, 659–672. <https://doi.org/10.1016/j.chembiol.2017.05.015>.
4. Feldkamp, L.A., Davis, L.C., and Kress, J.W. (1984). Practical cone-beam algorithm. *Josa a* **7**, 612–619.
5. Feldkamp, L.A., Goldstein, S.A., Parfitt, A.M., Jesion, G., and Kleerekoper, M. (1989). The direct examination of three-dimensional bone architecture in vitro by computed tomography. *J. Bone Miner. Res.* **4**, 3–11.
6. Franken, P.A., Hill, A.E., Peters, C.W., and Weinreich, G. (1961). Generation of optical harmonics. *Phys. Rev. Lett.* **7**, 118–119.
7. Freund, I., and Deutsch, M. (1986). Second-harmonic microscopy of biological tissue. *Opt. Lett.* **11**, 94–96.
8. Odeblad, E., and Lindström, G. (1955). Some preliminary observations on the proton magnetic resonance in biologic samples. *Acta radiol.* **43**, 469–476.
9. Iglesias, J.E., Augustinack, J.C., Nguyen, K., Player, C.M., Player, A., Wright, M., Roy, N., Frosch, M.P., McKee, A.C., Wald, L.L., et al. (2015). A computational atlas of the hippocampal formation using ex vivo, ultra-high resolution MRI: application to adaptive segmentation of in vivo MRI. *Neuroimage* **115**, 117–137.
10. Gong, H., Xu, D., Yuan, J., Li, X., Guo, C., Peng, J., Li, Y., Schwarz, L.A., Li, A., Hu, B., et al. (2016). High-throughput dual-colour precision imaging for brain-wide connectome with cytoarchitectonic landmarks at the cellular level. *Nat. Commun.* **7**, 12142. <https://doi.org/10.1038/ncomms12142>.
11. Economo, M.N., Clack, N.G., Lavis, L.D., Gerfen, C.R., Svoboda, K., Myers, E.W., and Chandrashekar, J. (2016). A platform for brain-wide imaging and reconstruction of individual neurons. *Elife* **5**, e10566. <https://doi.org/10.7554/eLife.10566>.
12. Ragan, T., Kadiri, L.R., Venkataraju, K.U., Bahlmann, K., Sutini, J., Taranda, J., Arganda-Carreras, I., Kim, Y., Seung, H.S., and Osten, P. (2012). Serial two-photon tomography for automated ex vivo mouse brain imaging. *Nat. Methods* **9**, 255–258. <https://doi.org/10.1038/nmeth.1854>.
13. Richardson, D.S., Guan, W., Matsumoto, K., Pan, C., Chung, K., Ertürk, A., Ueda, H.R., and Lichtman, J.W. (2021). Tissue clearing. *Nat. Rev. Methods Primers* **1**, 84. <https://doi.org/10.1038/s43586-021-00080-9>.
14. Tainaka, K., Kuno, A., Kubota, S.I., Murakami, T., and Ueda, H.R. (2016). Chemical principles in tissue clearing and staining protocols for whole-body cell profiling. *Annu. Rev. Cell Dev. Biol.* **32**, 713–741. <https://doi.org/10.1146/annurev-cellbio-111315-125001>.
15. Richardson, D.S., and Lichtman, J.W. (2015). Clarifying tissue clearing. *Cell* **162**, 246–257. <https://doi.org/10.1016/j.cell.2015.06.067>.
16. Kim, S.Y., Cho, J.H., Murray, E., Bakh, N., Choi, H., Ohn, K., Ruelas, L., Hubbert, A., McCue, M., Vassallo, S.L., et al. (2015). Stochastic electro-transport selectively enhances the transport of highly electromobile molecules. *Proc. Natl. Acad. Sci. USA* **112**, E6274–E6283. <https://doi.org/10.1073/pnas.1510133112>.
17. Susaki, E.A., Shimizu, C., Kuno, A., Tainaka, K., Li, X., Nishi, K., Morishima, K., Ono, H., Ode, K.L., Saeki, Y., et al. (2020). Versatile whole-organ/body staining and imaging based on electrolyte-gel properties of biological tissues. *Nat. Commun.* **11**, 1982. <https://doi.org/10.1038/s41467-020-15906-5>.
18. Lai, H.M., Tang, Y., Lau, Z.Y.H., Campbell, R.A.A., Yau, J.C.N., Chan, C.C.Y., Chan, D.C.W., Wong, T.Y., Wong, H.K.T., Yan, L.Y.C., et al. (2022). Antibody stabilization for thermally accelerated deep immunostaining. *Nat. Methods* **19**, 1137–1146. <https://doi.org/10.1038/s41592-022-01569-1>.
19. Renier, N., Wu, Z., Simon, D.J., Yang, J., Ariel, P., and Tessier-Lavigne, M. (2014). iDISCO: a simple, rapid method to immunolabel large tissue samples for volume imaging. *Cell* **159**, 896–910. <https://doi.org/10.1016/j.cell.2014.10.010>.
20. Zhao, S., Todorov, M.I., Cai, R., Maskari, R.A., Steinke, H., Kemter, E., Mai, H., Rong, Z., Warmer, M., Stanic, K., et al. (2020). Cellular and molecular probing of intact human organs. *Cell* **180**, 796–812.e19. <https://doi.org/10.1016/j.cell.2020.01.030>.
21. Cai, R., Pan, C., Ghasemigharagoz, A., Todorov, M.I., Förstera, B., Zhao, S., Bhatia, H.S., Parra-Damas, A., Mrowka, L., Theodorou, D., et al. (2019). Panoptic imaging of transparent mice reveals whole-body neuronal projections and skull-meninges connections. *Nat. Neurosci.* **22**, 317–327. <https://doi.org/10.1038/s41593-018-0301-3>.
22. Ku, T., Guan, W., Evans, N.B., Sohn, C.H., Albanese, A., Kim, J.G., Frosch, M.P., and Chung, K. (2020). Elasticizing tissues for reversible shape transformation and accelerated molecular labeling. *Nat. Methods* **17**, 609–613. <https://doi.org/10.1038/s41592-020-0823-y>.
23. Murray, E., Cho, J.H., Goodwin, D., Ku, T., Swaney, J., Kim, S.Y., Choi, H., Park, Y.G., Park, J.Y., Hubbert, A., et al. (2015). Simple, scalable proteomic imaging for high-dimensional profiling of intact systems. *Cell* **163**, 1500–1514. <https://doi.org/10.1016/j.cell.2015.11.025>.
24. Yun, D.H., Park, Y.-G., Cho, J.H., Kamentsky, L., Evans, N.B., Albanese, A., Xie, K., Swaney, J., Sohn, C.H., Tian, Y., et al. (2019). Ultrafast immunostaining of organ-scale tissues for scalable proteomic phenotyping. Preprint at bioRxiv. <https://doi.org/10.1101/660373>.
25. Johnstone, R.W., Andrew, S.M., Hogarth, M.P., Pietersz, G.A., and McKenzie, I.F. (1990). The effect of temperature on the binding kinetics and equilibrium constants of monoclonal antibodies to cell surface antigens. *Mol. Immunol.* **27**, 327–333. [https://doi.org/10.1016/0161-5890\(90\)90045-2](https://doi.org/10.1016/0161-5890(90)90045-2).
26. Reverberi, R., and Reverberi, L. (2007). Factors affecting the antigen-antibody reaction. *Blood Transfus* **5**, 227–240. <https://doi.org/10.2450/2007.0047-07>.
27. Ejima, D., Tsumoto, K., Fukada, H., Yumioka, R., Nagase, K., Arakawa, T., and Philo, J.S. (2007). Effects of acid exposure on the conformation, stability, and aggregation of monoclonal antibodies. *Proteins* **66**, 954–962. <https://doi.org/10.1002/prot.21243>.
28. Quatieri, L.F., Anderson, A.G., and Meyers, P. (1977). Effects of ionic and nonionic detergents on antigen-antibody reactions. *J. Immunol.* **119**, 1645–1651.
29. Crumpton, M.J., and Parkhouse, R.M. (1972). Comparison of the effects of various detergents on antigen-antibody interaction. *FEBS Lett.* **22**, 210–212. [https://doi.org/10.1016/0014-5793\(72\)80047-4](https://doi.org/10.1016/0014-5793(72)80047-4).
30. Kirley, T.L., Greis, K.D., and Norman, A.B. (2018). Domain unfolding of monoclonal antibody fragments revealed by non-reducing SDS-PAGE. *Biochem. Biophys. Rep.* **16**, 138–144. <https://doi.org/10.1016/j.bbrep.2018.10.004>.
31. Dimitriadis, G.J. (1979). Effect of detergents on antibody-antigen interaction. *Anal. Biochem.* **98**, 445–451. [https://doi.org/10.1016/0003-2697\(79\)90165-9](https://doi.org/10.1016/0003-2697(79)90165-9).
32. Berg, H.C. (1993). *Random Walks in Biology* (Princeton University Press).
33. Li, J., Czajkowsky, D.M., Li, X., and Shao, Z. (2015). Fast immuno-labeling by electrophoretically driven infiltration for intact tissue imaging. *Sci. Rep.* **5**, 10640. <https://doi.org/10.1038/srep10640>.
34. Renier, N., Wu, Z., Simon, D.J., Yang, J., Ariel, P., and Tessier-Lavigne, M. (2014). iDISCO: a simple, rapid method to immunolabel large tissue samples for volume imaging. *Cell* **159**, 896–910. <https://doi.org/10.1016/j.cell.2014.10.010>.
35. Pan, C., Cai, R., Quacquarelli, F.P., Ghasemigharagoz, A., Loubopoulos, A., Matryba, P., Plesnila, N., Dichgans, M., Hellal, F., and Ertürk, A. (2016). Shrinkage-mediated imaging of entire organs and organisms using uDISCO. *Nat. Methods* **13**, 859–867. <https://doi.org/10.1038/nmeth.3964>.
36. Poša, M., and Sebenji, A. (2014). Determination of number-average aggregation numbers of bile salts micelles with a special emphasis on their oxo derivatives—the effect of the steroid skeleton. *Biochim. Biophys. Acta* **1840**, 1072–1082. <https://doi.org/10.1016/j.bbagen.2013.11.008>.
37. Hama, H., Kurokawa, H., Kawano, H., Ando, R., Shimogori, T., Noda, H., Fukami, K., Sakaue-Sawano, A., and Miyawaki, A. (2011). Scale: a chemical approach for fluorescence imaging and reconstruction of transparent

- mouse brain. *Nat. Neurosci.* *14*, 1481–1488. <https://doi.org/10.1038/nn.2928>.
38. Tainaka, K., Murakami, T.C., Susaki, E.A., Shimizu, C., Saito, R., Takahashi, K., Hayashi-Takagi, A., Sekiya, H., Arima, Y., Nojima, S., et al. (2018). Chemical landscape for tissue clearing based on hydrophilic reagents. *Cell Rep.* *24*, 2196–2210.e9. <https://doi.org/10.1016/j.celrep.2018.07.056>.
39. Chen, F., Tillberg, P.W., and Boyden, E.S. (2015). Optical imaging. Expansion microscopy. *Science* *347*, 543–548. <https://doi.org/10.1126/science.1260088>.
40. Ku, T., Swaney, J., Park, J.Y., Albanese, A., Murray, E., Cho, J.H., Park, Y.G., Mangena, V., Chen, J., and Chung, K. (2016). Multiplexed and scalable super-resolution imaging of three-dimensional protein localization in size-adjustable tissues. *Nat. Biotechnol.* *34*, 973–981. <https://doi.org/10.1038/nbt.3641>.
41. Freitas, R.A. (1999). *Nanomedicine, Volume I: Basic Capabilities* (Landes Bioscience Georgetown, TX).
42. Park, Y.G., Sohn, C.H., Chen, R., McCue, M., Yun, D.H., Drummond, G.T., Ku, T., Evans, N.B., Oak, H.C., Trieu, W., et al. (2018). Protection of tissue physicochemical properties using polyfunctional crosslinkers. *Nat. Biotechnol.* *37*, 73–83. <https://doi.org/10.1038/nbt.4281>.
43. Kirst, C., Skriabine, S., Vieites-Prado, A., Topilko, T., Bertin, P., Gerschenfeld, G., Verry, F., Topilko, P., Michalski, N., Tessier-Lavigne, M., and Renier, N. (2020). Mapping the fine-scale organization and plasticity of the brain vasculature. *Cell* *180*, 780–795.e25. <https://doi.org/10.1016/j.cell.2020.01.028>.
44. Hickey, J.W., Neumann, E.K., Radtke, A.J., Camarillo, J.M., Beuschel, R.T., Albanese, A., McDonough, E., Hatler, J., Wiblin, A.E., Fisher, J., et al. (2022). Spatial mapping of protein composition and tissue organization: a primer for multiplexed antibody-based imaging. *Nat. Methods* *19*, 284–295. <https://doi.org/10.1038/s41592-021-01316-y>.
45. Liu, Y., Beyer, A., and Aebersold, R. (2016). On the dependency of cellular protein levels on mRNA abundance. *Cell* *165*, 535–550. <https://doi.org/10.1016/j.cell.2016.03.014>.
46. Rangaraju, V., Tom Dieck, S., and Schuman, E.M. (2017). Local translation in neuronal compartments: how local is local? *EMBO Rep.* *18*, 693–711. <https://doi.org/10.15252/embr.201744045>.
47. Chen, W.T., Lu, A., Craessaerts, K., Pavie, B., Sala Frigerio, C., Corthout, N., Qian, X., Laláková, J., Kühnemund, M., Voytyuk, I., et al. (2020). Spatial transcriptomics and in situ sequencing to study alzheimer’s disease. *Cell* *182*, 976–991.e19. <https://doi.org/10.1016/j.cell.2020.06.038>.
48. Anishchenko, I., Pellock, S.J., Chidyausiku, T.M., Ramelot, T.A., Ovchinnikov, S., Hao, J., Bafna, K., Norn, C., Kang, A., Bera, A.K., et al. (2021). De novo protein design by deep network hallucination. *Nature* *600*, 547–552. <https://doi.org/10.1038/s41586-021-04184-w>.
49. Cao, L., Coventry, B., Goreshnik, I., Huang, B., Sheffler, W., Park, J.S., Jude, K.M., Marković, I., Kadam, R.U., Verschueren, K.H.G., et al. (2022). Design of protein-binding proteins from the target structure alone. *Nature* *605*, 551–560. <https://doi.org/10.1038/s41586-022-04654-9>.